

Journal of Materials Chemistry A

Materials for energy and sustainability

Accepted Manuscript

This article can be cited before page numbers have been issued, to do this please use: S. Patil, H. Chou, Y. Chen, S. Hsieh, C. Chen, C. Chang, S. Li, Y. Lee, Y. Lin, H. Li, Y. J. Chang, Y. Lai and D. Wang, *J. Mater. Chem. A*, 2020, DOI: 10.1039/D0TA10696H.



This is an Accepted Manuscript, which has been through the Royal Society of Chemistry peer review process and has been accepted for publication.

Accepted Manuscripts are published online shortly after acceptance, before technical editing, formatting and proof reading. Using this free service, authors can make their results available to the community, in citable form, before we publish the edited article. We will replace this Accepted Manuscript with the edited and formatted Advance Article as soon as it is available.

You can find more information about Accepted Manuscripts in the [Information for Authors](#).

Please note that technical editing may introduce minor changes to the text and/or graphics, which may alter content. The journal's standard [Terms & Conditions](#) and the [Ethical guidelines](#) still apply. In no event shall the Royal Society of Chemistry be held responsible for any errors or omissions in this Accepted Manuscript or any consequences arising from the use of any information it contains.

Enhanced N₂ Affinity of 1T-MoS₂ with Unique Pseudo Six-membered Ring Consisting of N—Li—S—Mo—S—Mo for High Ambient Ammonia Electrosynthesis Performance

Shivaraj B. Patil,^{1#} Hung-Lung Chou,^{2#} Yu-Mei Chen,¹ Shang-Hsien Hsieh,³ Chia-Hao Chen,³ Chia-Che Chang,¹ Shin-Ren Li,¹ Yi-Cheng Lee,¹ Ying-Sheng Lin,¹ Hsin Li,¹ Yuan Jay Chang,¹ Ying-Huang Lai,¹ Di-Yan Wang^{1*}

¹ Department of Chemistry, Tunghai University, Taichung 40704, Taiwan

² Graduate Institute of Applied Science and Technology, National Taiwan University of Science and Technology, Taipei 10607, Taiwan

³ National Synchrotron Radiation Research Center, Hsinchu 30076, Taiwan

#Shivaraj B. Patil and Hung-Lung Chou contributed equally to this work

Corresponding author: diyanwang@thu.edu.tw

Abstract

The Haber–Bosch process is widely used to convert atmospheric nitrogen (N₂) into ammonia (NH₃). However, the extreme reaction conditions and abundant carbon released by this process make it important to develop a greener NH₃ production method. The electrochemical nitrogen reduction reaction (NRR) is an attractive alternative to the Haber–Bosch process. Herein, we demonstrated that molybdenum sulfide on nickel foil (1T-MoS₂-Ni) with low crystallinity was an active NRR electrocatalyst. 1T-MoS₂-Ni achieved a high faradaic efficiency of 27.66% for the NRR at –0.3 V (vs. RHE) in LiClO₄ electrolyte. In-situ X-ray diffraction and ex-situ X-ray photoemission analyses showed that lithium ions intercalated into the 1T-MoS₂ layers during the NRR. Moreover, theoretical calculations revealed the differences between six membered rings formed in the 1T-MoS₂ and 2H-MoS₂ systems with Li intercalation. The bond distances of d(Mo—N) and d(N—Li) of in Li-1T-MoS₂ were found to be shorter than those in Li-2H-MoS₂, resulting in a lower energy barrier of N₂ fixation and higher NRR activity. Therefore, 1T-MoS₂-Ni is promising as a scalable and low-cost NRR electrocatalyst with lower power consumption and carbon emission than the Haber–Bosch process.

Keywords: 1T-MoS₂, Nitrogen Reduction Reaction, Pseudo Six-member Ring, in-situ X-ray diffraction, Lithium Interactions

Introduction

Ammonia (NH₃) has attracted extensive interest for over a century because of its wide range of applications, including as a green fertilizer and non-carbon fuel for vehicles.¹⁻³ Although nitrogen (N₂) is the most abundant gas in the Earth's atmosphere, it is metabolically useless unless nitrogen fixation is carried out. The electrocatalytic nitrogen reduction reaction (NRR) is a promising process that breaks the triple bond of N₂ with suitable catalysts to form NH₃ ($\text{N}_2 + 6\text{H}^+ + 6\text{e}^- \rightarrow 2\text{NH}_3$).⁴⁻⁷ There are three main factors that need to be considered to optimize electrocatalysts for the NRR: (1) the adsorption ability of N₂ on the catalyst surface, (2) reaction selectivity to suppress the hydrogen evolution reaction (HER), and (3) the compatibility and stability of materials.^{8,9} It is important to develop new catalysts that acceptably address these factors to realize highly efficient electrochemical N₂ reduction to NH₃.

Recently, many metal sulfides such as 2H-MoS₂,¹⁰ FeS₂,¹¹ and SnS₂¹² have been investigated as catalysts for the NRR. However, metal sulfides show low faradaic efficiency (FE) in the NRR,¹³⁻¹⁵ which has been attributed to poor N₂ adsorption on their surface and the inability to effectively suppress the HER. Understanding the detailed reaction mechanism of these catalysts could provide direction to design more active NRR catalysts. The electrochemical properties and reaction pathway of FeS₂ in the NRR were studied experimentally and by density functional theory (DFT) simulations.¹¹ The results showed that Fe atoms acted as NRR active centres and greatly lowered the energy barrier for the NRR. Sun et al.¹⁶ revealed that Mo atoms were the NRR active centres of 2H-MoS₂, which displayed an FE of 1.2%. MoS₂ was decorated with Ru clusters to provide extra binding sites for N₂ activation for the NRR, resulting in an FE of 18%.¹⁷

Increasing catalyst surface activity through atomic manipulation is a promising direction to raise the FE of the electrochemical NRR. The preparation of metal oxides or sulfides with high metallic surface exposure to increase NRR activity has been proposed.¹⁸ For example, Xin and co-workers achieved an FE of 14.6% (3.6 μg/h/mg_{cat}) for atomically dispersed Mo atoms on N-doped porous carbon.¹⁹ The high FE and NH₃ yield of this catalyst were attributed to its high metal exposure, which facilitated N₂ adsorption.

It has also been found that low crystalline (amorphous) materials show enhanced NRR activity over their crystalline counterparts, which is attributed to the dangling bonds of low crystalline materials acting as unsaturated coordination sites for N₂ adsorption.²⁰ For example, Yan et al.²¹ found that low crystalline Au on Ce_xO₂-reduced graphene oxide exhibited an FE of 10.10%, which was much higher than that of its crystalline counterpart (3.67%). The improved NRR activity was ascribed to the low crystalline structure providing more active sites for N₂ adsorption than the corresponding crystalline structure.

Recently, 1T-MoS₂ has emerged as a promising material for a wide range of electrochemical applications because of its metallic properties and highly active surface, which is composed of a single layer of S-Mo-S structure in which Mo is linked to six S atoms to form an octahedral lattice.²²⁻²⁴ This structure endows 1T-MoS₂ with abundant active sites and high electronic conductivity (six orders of magnitude higher than that of 2H-MoS₂).²² These characteristics facilitate the exclusive interactions of ions/molecules dissolved in an electrolyte with a 1T-MoS₂ catalyst and the rapid diffusion of ions.²⁵ The dense active sites of 1T-MoS₂ promote catalytic activity and its high electronic conductivity affords fast electron transfer.²⁴ Indeed, 1T-MoS₂ has been used as an active catalyst for the HER.^{22, 23} To design an active 1T-MoS₂ NRR electrocatalyst, its HER activity needs to be suppressed and N₂ adsorption ability needs to be increased.

The NRR efficiency of 1T-MoS₂ might be increased by forming new intermolecular interactions in the MoS₂ structure to facilitate N₂ adsorption. For example, the FE of 2H-MoS₂ was increased by the formation of an additional Li-S bond in its crystal structure during Li⁺ intercalation.²⁵ The FE of this structure was 9.8%, which still has room for improvement. Because 1T-MoS₂ has a different crystal structure from that of 2H-MoS₂, it could form different intermolecular interactions with Li⁺, which could modify its NRR catalytic activity. In this work, to further improve the NRR catalytic performance of 1T-MoS₂, low crystalline 1T-MoS₂ grown on nickel foil (denoted as 1T-MoS₂-Ni) is designed as a robust electrocatalyst for the NRR. The performance of 1T-MoS₂-Ni as an NRR electrocatalyst in LiClO₄ electrolyte is investigated. In-situ X-ray diffraction (XRD) and ex-situ X-ray photoelectron spectroscopy (XPS) measurements are carried out to examine the intercalation of Li into 1T-MoS₂. A detailed reaction pathway for Li-intercalated 1T-MoS₂ (Li-1T-MoS₂) in the NRR is also elucidated.

Results and Discussion

To study the differences between the catalytic mechanisms of N₂ reduction on the surface of Li-1T-MoS₂ and Li-intercalated 2H-MoS₂ (Li-2H-MoS₂), model optimization was performed in 14×14×20 Å³ systems by DFT calculations, as shown in **Figure 1(a) and (b)**, respectively. The calculated N₂ adsorption energies at the Mo and S sites of the intrinsic 1T-MoS₂ and Mo sites of Li-1T-MoS₂ and Li-2H-MoS₂ are listed in **Table 1**. The active site for N₂ adsorption on 1T-MoS₂ is Mo because the Mo site possesses a negative N₂ adsorption energy (−0.28 eV). The N₂ adsorption energies on Li-1T-MoS₂ and Li-2H-MoS₂ were −0.72 and −0.70 eV, respectively, indicating their much stronger ability to adsorb N₂ than that of intrinsic 1T-MoS₂. These results indicated that N₂ adsorption on the 1T-MoS₂ or 2H-MoS₂ surface was strongly affected by the specific interactions of Li and S atoms, which is consistent with the findings of a previous report.²⁶ To study the suppression of hydrogen adsorption on S site in Li-1T-MoS₂, DFT calculation was also performed in Table S1. The results indicated that the hydrogen (H*) adsorption free

energies (ΔG^{H*}) of 0.03 eV was obtained on S-edge sites of pristine MoS₂ system. In contrast, with Li-S interactions, the ΔG^{H*} increased dramatically to 0.49 eV on S-edge sites of Li-MoS₂ system. The result represented that S-edge sites in pristine MoS₂ system were more favorable for HER than that of Li-MoS₂ thermodynamically. Therefore, the Li-S bond can efficiently suppress the HER on the S atoms of MoS₂, which are believed to behave as the active sites for the HER.^{16, 26-29}

After geometry relaxation, the optimized calculated distance of N₂ in Li-1T-MoS₂ and Li-2H-MoS₂ (Figure 1 (a) and (b), respectively) showed that a pseudo six-membered ring containing the interaction N...Li...S—Mo—S—Mo formed. The N...Li interaction in the six-membered ring is believed to enhance the N₂ adsorption ability on the surface of MoS₂ and possibly weaken the N≡N bond to improve the conversion efficiency of the NRR. Comparison of the Li-1T-MoS₂ and Li-2H-MoS₂ systems revealed that the bond distances of $d(\text{Mo—N})$ of ~ 1.797 Å and $d(\text{N—Li})$ of ~ 2.119 Å in Li-1T-MoS₂ were shorter than $d(\text{Mo—N})$ of ~ 2.010 Å and $d(\text{N—Li})$ of ~ 2.639 Å in Li-2H-MoS₂, respectively. These results indicate that the N₂ adsorption ability of Li-1T-MoS₂ is stronger than that of Li-2H-MoS₂. In other words, the Li-1T-MoS₂ system should facilitate the formation of N-H bonds. Directed by these results, we fabricated and characterized Li-1T-MoS₂ as an NRR electrocatalyst.

Thiourea has been widely used as a sulfur source in the conventional synthesis of organic/inorganic compounds because of its high sulfur content, easy release of sulfur, and low cost, even though it is recognized as a toxic chemical. To make our catalyst fabrication as green and eco-friendly as possible, herein, 1T-MoS₂-Ni was fabricated by immersing pre-treated (acid-washed) Ni foil in a solution containing molybdic acid and a minimal amount of thiourea through a facile hydrothermal process. **Figure 2(a)** shows the XRD pattern of 1T-MoS₂-Ni, which indicates that 1T-MoS₂-Ni has low crystallinity with two peaks at 9.0° and 18.72° corresponding to the (002) and (004) planes of 1T-MoS₂, respectively, in agreement with the literature.³⁰ These results were attributed to the formation of low crystalline 1T-MoS₂ on Ni foil. In contrast, 1T-MoS₂ grown on carbon fiber paper (1T-MoS₂-CFP) and 1T-MoS₂ grown on Ti foil (1T-MoS₂-Ti) displayed higher crystalline structures with peaks from the same planes observed in their XRD patterns (see the supporting information). Figure S1(d-e) show the Raman spectra of 1T-MoS₂ grown on different substrates and confirm the formation of 1T-MoS₂ with low crystallinity over Ni foil.^{23, 31, 32} A scanning electron microscopy (SEM) image of 1T-MoS₂-Ni is shown in **Figure 2(b)**. It reveals that the 1T-MoS₂-Ni consists of particles with rough surfaces. In contrast, 1T-MoS₂-CFP consisted of sheet structure with high crystallinity (Figure S2). To analyze the element distribution of 1T-MoS₂-Ni, energy-dispersive X-ray spectroscopy (EDX) elemental mapping analysis was carried out. **Figure 2(c)** shows a cross-sectional SEM image of 1T-MoS₂-Ni, which clearly illustrates that the 1T-MoS₂ is attached to the Ni foil. **Figure 2(d)–(g)** show related EDX mapping of 1T-MoS₂-Ni,

which confirmed the uniform distributions of Mo and S on Ni. The few signals from oxygen (Figure 1(h)) could originate from the chemisorption of atmospheric oxygen.

To investigate the catalytic activity of 1T-MoS₂-Ni in the NRR, electrochemical experiments were conducted in N₂-saturated 0.25 M LiClO₄. The electrochemical reactions were carried out in an H-type cell in which the counter and working electrodes were separated by a Nafion membrane. Platinum wire (Pt) and a saturated calomel electrode (SCE) were used as counter and reference electrodes, respectively. All potentials are referenced to the reversible hydrogen electrode (RHE). **Figure 3(a)** presents the results of linear sweep voltammetry (LSV) performed at a scan rate of 10 mV/s to determine the possible electrochemical window for the NRR over 1T-MoS₂-Ni. A current density of 10 mA/cm² was obtained at an applied voltage of -0.6 V (vs. RHE). To investigate the dependence of the electrochemical NRR by the 1T-MoS₂-Ni electrocatalyst on potential, constant-current curves were measured at different voltages of -0.2 to -0.6 V for 40 min, as shown in **Figure 3(b)**. The current density increased from 2.0 to 10.0 mA/cm² as the applied voltage changed from -0.2 to -0.6 V. Interestingly, no bubbles were observed in the range from -0.2 V to -0.6 V, meaning that hydrogen evolution on the surface of catalysts was suppressed substantially.

To detect and quantify the NH₃ formed during the electrocatalytic NRR over 1T-MoS₂-Ni at different potentials, indophenol was added as an indicator and measured by ultraviolet-visible (UV-Vis) absorption spectroscopy. **Figure 3(c)** shows UV-Vis absorption spectra of the electrolytes colored with indophenol. The results showed that the highest absorption intensity was around 0.40 a.u. at -0.3 V and the lowest was ~0.03 a.u. at -0.2 V. To further confirm the generation of NH₃ over the 1T-MoS₂-Ni electrocatalyst, ¹H nuclear magnetic resonance (NMR) spectra were obtained, as presented in **Figure 3(d)**. The sample for NMR measurements was produced using a mixture of ¹⁴N₂ and ¹⁵N₂ as the gas source in 0.25 M LiClO₄ at -0.3 V (vs. RHE) for 4 h. The ¹H NMR spectrum clearly showed ¹⁴NH₄⁺ and ¹⁵NH₄⁺ signals, illustrating that NH₃ was produced by electrolysis over the 1T-MoS₂-Ni catalyst.

The NH₃ yields and related FE of 1T-MoS₂-Ni at given voltages are plotted in **Figure 3(e)**. At -0.2 V, the catalyst exhibited an FE of 11.57% and produced NH₃ at a rate of 0.11 μg/min, whereas it achieved its highest FE of 27.66% with an NH₃ yield rate of 1.05 μg/min/cm² at -0.3 V. Beyond -0.3 V, FE decreased at more negative potential (8.02% at -0.4 V, 4.32% at -0.5 V, and 0.70% at -0.6 V). This phenomenon may be ascribed to the domination of the HER over the NRR at more negative potential. The formation of hydrazine during the reaction was not detected (**Figure S3**). Griess test of electrolyte and gas chromatography of N₂ gas were also performed to check the NO_x contamination and no contamination was found. (**Figure S3, S4**). Furthermore, controlled experiments were performed to show no effect of counter electrodes, anions of the salt and Ni foil on NRR as shown in **Figure S5**.

To validate the effects of the 1T phase of 1T-MoS₂-Ni with low crystallite nature on its performance as an NRR electrocatalyst, 1T-MoS₂-CFP and 1T-MoS₂-Ti with highly crystalline structures were fabricated (**Figure S1 and S2**). In addition, 2H-MoS₂-CFP was also prepared by annealing 1T-MoS₂-CFP at high temperature in sulfur vapor. The structure characterization of 1T-MoS₂-CFP, 1T-MoS₂-Ti, and 2H-MoS₂-CFP is provided in the Supporting Information. All electrochemical tests were carried out in 0.25 M LiClO₄ electrolyte at -0.3 V. **Figure 3(f)** shows that 1T-MoS₂-CFP, 1T-MoS₂-Ti, and 2H-MoS₂-CFP with high crystallinity only achieved FEs of 12.24%, 10.5%, and 8.06%, respectively, in the NRR. These results confirm that the low crystallite nature of 1T-MoS₂-Ni leads to its high FE in the NRR by providing abundant active sites. **Table S2** compares the performance of 1T-MoS₂-Ni with that of other reported metal sulfide NRR electrocatalysts.

To validate the stability of 1T-MoS₂-Ni, long term measurements and multiple cycles of the NRR were conducted. Long-term electrocatalytic NRR was carried out for 13 h at -0.3 V. **Figure 4(a)** shows the time-dependent current curve of 1T-MoS₂-Ni at -0.3 V for 13 h. The corresponding absorption spectrum (inset of Figure 3(a)) reveals that the absorption intensity of indophenol was 1.99 a.u. after 13 h. After 13 h of electrocatalysis, the FE of 1T-MoS₂-Ni was still 26.47%. **Figure 4(b)** displays the data obtained from consecutive electrochemical cycling tests. The NRR was conducted at -0.3 V for 40 min five times using the same 1T-MoS₂-Ni sample. Both FE and NH₃ yield rate remained similar over the five cycles (corresponding time-dependent current curves and UV-Vis spectra are provided in **Figure S6**). Overall, these results indicated that 1T-MoS₂-Ni demonstrated remarkably stable catalytic activity in the NRR.

The intercalation/interaction of Li⁺ with MoS₂/S₂⁻ has been recognized as another factor that can raise the NRR activity of 2H-MoS₂.²⁶ To investigate the Li⁺ intercalation of 1T-MoS₂ during the electrochemical NRR in LiClO₄ electrolyte, XPS and in-situ XRD measurements were performed (see **Figure S7** for the in-situ XRD setup). Intrinsic 1T-MoS₂ and 2H-MoS₂ with no Li intercalation were used as reference samples for comparison. **Figure 5(a), (b), and (c)** show Mo 3d, S 2p, and Li 1s spectra, respectively, for the samples. Two characteristic peaks from Mo 3d_{5/2} and Mo 3d_{3/2} were clearly identified in the Mo 3d spectrum of MoS₂. These peaks of intrinsic 1T-MoS₂ were shifted to lower binding energy compared with those of 2H-MoS₂ (**Figure 5(a)**). Similarly, the peaks ascribed to 2P_{1/2} and 2P_{3/2} in the S 2p spectrum of intrinsic 1T-MoS₂ were also shifted to lower binding energy compared with those of 2H-MoS₂ (**Figure 5(b)**). The lower binding energies of Mo and S for intrinsic 1T-MoS₂ than for 2H-MoS₂ can be attributed to the increased electron density of the Mo and S atoms of 1T-MoS₂ compared with the case for 2H-MoS₂.^{22, 24, 25, 30, 33, 34} After electrolysis at -0.3 V for 40 min, the Mo 3d and S 2p peaks of 1T-MoS₂-Ni slightly shifted to lower and higher energy, respectively, indicating that the oxidation state of S

atoms of 1T-MoS₂-Ni was higher than that of intrinsic 1T-MoS₂. This result was attributed to the intercalation of Li⁺ into 1T-MoS₂-Ni to form Li-1T-MoS₂-Ni, resulting in the formation of Li-S bonds.^{26, 34} **Figure 5(c)** shows the rise of the Li 1s peak of Li-1T-MoS₂-Ni, further substantiating the intercalation of Li⁺ into 1T-MoS₂.

Figure 5(d) displays selected XRD patterns of 1T-MoS₂-CFP collected during the NRR in LiClO₄ electrolyte with a linear scan from 0 to -0.6 V. We chose 1T-MoS₂-CFP for in-situ XRD studies because its higher crystallinity than that of 1T-MoS₂-Ni facilitated observation of its structural transformation. The corresponding linear scan is shown in **Figure 5(e)**. The results reveal that the peak observed at 9.5° for 1T-MoS₂ shifted to 7° at more negative potential, confirming that Li⁺ was intercalated into the 1T-MoS₂ layers.³⁵ To further study the role of Li⁺ in the NRR activity of Li-1T-MoS₂-Ni, Na₂SO₄ was used as the electrolyte in the NRR. **Figure 5(f)** shows the FE of Li-1T-MoS₂-Ni, intrinsic 1T-MoS₂, and 2H-MoS₂ electrocatalysts operated in 0.25 M NaSO₄ electrolyte at -0.3 V for 40 min. The corresponding current-dependent curves and UV-Vis spectra are provided in **Figure S8**. Interestingly, Li-1T-MoS₂-Ni exhibited a higher FE compared with those of intrinsic 1T-MoS₂ and 2H-MoS₂. Further, post catalytic characterizations including XRD and SEM of 1T-MoS₂-Ni (**Figure S9**) revealed that 1T phase with low crystallite nature remains unchanged. Owing to Li intercalation into MoS₂ matrix, shift of dominant peak in XRD from 9° to 7° was also observed. Overall, these results confirmed the influence of Li⁺ on the NRR activity of MoS₂. The role of Li⁺ in increasing the FE of MoS₂ was further examined by DFT simulations.

To investigate the catalytic mechanism of Li-1T-MoS₂ in the NRR compared with those of intrinsic 1T-MoS₂ and Li-intercalated 2H-MoS₂ (Li-2H-MoS₂), DFT calculations were performed to determine their molecular structures and map potential energy diagrams of the NRR. In the models, N₂ was adsorbed on three kinds of MoS₂ slab surfaces consisting of one Li atom, 25 Mo atoms, and 46 S atoms, as shown in **Figure 6(a)**. The charge transfer between Mo, S, and Li atoms in Li-1T-MoS₂ was believed to be an important index that affects the adsorption ability of N₂ molecules and thus NRR activity. **Figure 6(b)** presents the representative electron contour map of Li-1T-MoS₂ and the calculated charge transfer values are listed in **Table 2**. The formation of Li-S bonds was predicted in this model. Our results clearly showed that charge transfer occurred from Li to S in the Li-1T-MoS₂ system. The charge on S increased from 6.73e for intrinsic 1T-MoS₂ to 6.96e for Li-1T-MoS₂ and the charge on Li decreased from 3.61e for bare Li to 2.16e for Li-1T-MoS₂. Therefore, the charge of an N atom of N₂ increased from 6.87e to 6.98e upon adsorption by Li-1T-MoS₂, which could affect the bond strength of N₂ and facilitate the NRR.

Figure 7 shows that the activation energy of the potential determining step for the NRR on intrinsic 1T-MoS₂, Li-1T-MoS₂, and Li-2H-MoS₂. For intrinsic 1T-MoS₂, an energy barrier of +0.79 eV was found

for the reductive protonation of adsorbed N_2 (*NNH formation) without external potential. The energy barriers of the reductive protonation step for Li-intercalated 1T- and 2H-MoS₂ were much smaller than that for intrinsic 1T-MoS₂. In addition, the potentials of *NN adsorption (−0.72 eV) and *NNH formation (−0.23 eV) for Li-1T-MoS₂ were slightly lower than those for Li-2H-MoS₂ (−0.68 and −0.19 eV, respectively). In this step for the Li-1T-MoS₂ system, the N-N bond length increased from 1.18 Å in *N₂ to 1.23 Å *NNH. Therefore, the deformation charge density (Figure 6(b)) clearly illustrated the charge transfer from N₂ to a positively charged Mo atom, resulting in the formation of an N-Mo bond and notable weakening of the N≡N triple bond and facilitating the intermediate protonation reaction to form *NNH. Indeed, the opening of the inert triple bond of N₂ was the most energetically demanding step of the NRR, which is logical. Overall, our results indicated that the Li-1T-MoS₂ catalyst demonstrated a relatively low energy barrier for the NRR, making it a promising electrocatalyst for this challenging but important reaction.

Conclusion

We fabricated a high-performance 1T-MoS₂-Ni electrocatalyst for NRR with advantages including high exposure of metal active sites and high conductivity. The 1T-MoS₂-Ni electrocatalyst achieved an FE of 27.66% and generated NH₃ at a rate of 1.05 μg/min/cm² at −0.3 V in 0.25 M LiClO₄ electrolyte. DFT calculations indicated the formation of a pseudo six-membered ring with N₂ in the presence of Li⁺, which not only lowered the energy barrier for N₂ fixation but also effectively suppressed the HER through strong Li—S interactions. This work provides fundamental insights on electrocatalyst fabrication and interfacial chemistry between the electrode and electrolyte, which may act as a blueprint for developing advanced NRR electrocatalysts in the future.

Materials:

Molybdic acid (H₂MoO₄; ACS 85% min) and lithium perchlorate (LiClO₄; Analysis 99+%) were procured from Acros organics. Thiourea (CH₄N₂S; ACS 99+%), phenol (C₆H₅OH; ACS 100%), super P; (ACS 99+%), Nafion (5 wt%) and titanium (Ti; 99.99%) foil were procured from Sigma-Aldrich. Sodium hydroxide (NaOH; ACS 97+%) was procured from Shimakyu's pure chemicals. Sodium hypochlorite (NaClO; 6-14% active Cl basis) and sodium sulfate (Na₂SO₄; ACS 99+%) were procured from Honeywell-Fluka. Sodium pentacyanonitrosylferrate (III) dihydrate (Na₂[Fe(CN)₅NO].2H₂O; ACS 99+%) and lithium sulfate (Li₂SO₄; ACS 99.7%) were procured from Alfa Aesar. Nickel (Ni; 99.99%) foil was procured from MTI corporation whereas carbon fiber paper (CFP) was procured from CeTech Co., Ltd. ¹⁴N₂ (5N) and ¹⁵N₂ (98 atom % ¹⁵N) gases were procured from Toyo gas Co., Ltd., and Sigma-Aldrich, respectively. Distilled water and absolute ethanol were used throughout the experiments.

Fabrication of 1T-MoS₂ Nano-flowers:

1T-MoS₂ nano-flowers were fabricated by adopting simple hydrothermal method. Typically, 2.5 mM of H₂MoO₄ and 6.25 mM of CH₄N₂S were dissolved in 40 mL of distilled water and stirred vigorously for 30 min to form a homogeneous solution. The solution was then transferred to Teflon-lined stainless-steel autoclave and sealed it. The autoclave was heated to 180 °C for 24 h and then cooled to room temperature. The obtained product was washed for several times with DI-water and ethanol. The resulting sample was dried at 60 °C to obtain shiny black powder. The black powder was further characterized.

Fabrication of 1T-MoS₂ on CFP, Ni and Ti foils:

Similarly, 1T-MoS₂ on CFP, Ni and Ti foil were synthesized by placing CFP, Ni and Ti foil into the autoclave, respectively, and maintaining all procedure unchanged. Finally, the samples were dried at 60 °C and stored in a desiccator.

Fabrication of 1T-MoS₂ electrode catalyst:

Whereas, 1T-MoS₂ on Ni foil, CFP and Ti foil were used as it is by downsizing to 1 x 2 cm² area. During the electrochemical measurements, it was immersed into the electrolyte with an area of 1 x 1 cm².

Characterization:

XRD patterns were recorded by XRD instrument (Rigaku Miniflex 600). JEOL JSM-7800F and JEOL 2100F were used to capture FESEM and HRTEM images, respectively. X-ray photoemission spectroscopy (XPS) measurements were performed at the SPEM end station (BL09A) of the National Synchrotron Radiation Research Center (NSRRC).³⁶ The photon energy used to obtain Mo 3d, S 2p and Li 1s XPS spectra was 320 eV. The *in-situ* XRD measurement was taken with electrochemical cell under linear scan voltammetry method at a scan rate of 1 mV/s. The schematic setup is provided in the supporting information. In-situ XRD analysis was performed at the beamline of BL23A small/wide angle X-ray scattering (SWAXS) at Taiwan Light Source (TLS) and the beamline of 09A at the Taiwan Photon Source (TPS) in National Synchrotron Radiation Research Center.

Pretreatment prior to electrochemical measurements: Before each electrochemical measurement, all the units of electrochemical cell were boiled and rinsed several times in DI water and dried at 100 °C. Nafion membrane was used as received (no additional acid treatment). New membrane was used for each measurement to avoid contamination. Furthermore, all the labware including vials, pipet etc., were also rinsed DI water for several times. The ¹⁵N₂ and ¹⁴N₂ gases were passed through saturator (0.05 M H₂SO₄) for high purity. Ar was purged for 30 min prior to ¹⁵N₂ flow to expel inherent ¹⁴N₂.^{37, 38}

Electrochemical setup and measurements: The nitrogen reduction reactions were performed in a H-cell at ambient conditions. It consists of two cells separated by a Nafion 211 membrane. Reference and working electrodes were placed in single cell whereas counter electrode was placed in another cell. CHI-660 electrochemical analyzer with typical three electrode system was used to carry out all the electrochemical measurements. Herein, 1T-MoS₂-Ni was devised as working electrode whereas platinum rod (Pt) and saturated calomel electrode (SCE) were implemented as counter and reference electrodes, respectively. The potentials reported in this work were changed to RHE scale with the following equation: $E \text{ (vs. RHE)} = E \text{ (vs. SCE)} + 0.245 + 0.059 \times \text{pH}$. Subsequently, the current density was recorded with respect to geometric surface area of the working electrode. N₂-saturated 0.25 M LiClO₄ was used as an electrolyte in this work. All experiments were carried out at room temperature.

Ammonia (NH₃) detection:

Indophenol method with UV-vis spectroscopy was used to detect and quantify the yield amount of NH₃ in the solution. Briefly, 1 mL of electrolyte was collected from the cathodic cell and reacted with 100 μL of oxidizing solution containing NaClO (pCl=6-14) in 1 M NaOH. It was followed by the addition of 100 μL of 0.5 M phenol and 50 μL of catalyst solution containing 0.002 M Sodium nitropusside as the catalyst solution in turn. The solution mixture was mixed well gently for 30 s and kept still for 30 min in dark conditions. The absorbance measurements were recorded at $\lambda = 640 \text{ nm}$. NH₃ concentration was quantified by concentration-absorbance calibration curve. Standard NH₄Cl solution with NH₄⁺ concentrations 1, 2, 3, 4, 5, 6, 7, 8, 9, 10, 11, 12, 13, 14 and 15 $\mu\text{g/mL}$ in 0.25 M LiClO₄ were used to calibrate concentration-absorbance curve. The fitting curve ($y = 0.2952x + 0.008$, $R^2 = 0.9979$) found to be in linear coherence with the concentration of NH₃ (**Figure S10**). Similarly, it was done for Na₂SO₄ electrolyte also. NMR method was also carried out to support Indophenol test results (**Figure S10**). NMR calibration curve was obtained using equimolar concentration of ¹⁴NH₄⁺ and ¹⁵NH₄⁺ as shown in **Figure S11**.

NH₃ yield rate (Y_{NH3}) calculation:

$$\text{Yield rate}_{\text{mass}}(\text{NH}_3) = (c(\text{NH}_3) \times V) / (t \times A)$$

Where $c(\text{NH}_3)$ is the measured the concentration of NH₃, V is the volume of electrolyte, t is the duration time of the reduction reaction, and A is the geometric area of the cathode ($1 \times 1 \text{ cm}^2$).

Faradic efficiency (FE) calculation:

FE calculation in 0.25 M LiClO₄ electrolyte was carried out assuming that one NH₃ molecule is produced with 3 electrons. It can be represented as follows:

$$FE = (3F \times C_{\text{NH}_3} \times V) / (17 \times Q) \quad \text{Eq. 2}$$

Where, F stands for Faradaic constant (96485 C/mol) and Q stands for total quantity of supplied coulomb.

Hydrazine (N₂H₄) detection:

The Watt and Chrisp method was adopted to quantify the N₂H₄ in the electrolyte after the reaction.³⁹ The coloring agent was prepared by mixing 5.99 g of para-(dimethylamino) benzaldehyde (p-C₉H₁₁NO) with 30 mL of hydrochloric acid (HCl) and 300 mL of ethanol (C₂H₅OH). Briefly, 9 mL of 1.0 M HCl was added to 1 mL of electrolyte (after the reaction) and was followed by the addition of 5 mL of coloring agent. The absorbance measurements were recorded at $\lambda = 455$ nm after incubating for 30 min.

¹⁵N₂ Isotope labeling studies:

Using ¹⁵N₂ and ¹⁴N₂ as feeding gases, the ¹⁵N and ¹⁴N isotopic labeling studies were carried out, respectively. 99% enrichment of ¹⁵N in ¹⁵N₂ was supplied by Sigma-Aldrich. The ¹⁵N₂ and ¹⁴N₂ gases were passed through saturator (0.05 M H₂SO₄) for high purity. Briefly, electrocatalysis was carried out at 0.3 V for 4 h with continuously purging saturated a ¹⁵N₂ gas in the electrolyte (0.25 M LiClO₄). After the reaction, the reaction solution was concentrated to 2.0 mL at 80 °C for 3 hr. The pH of the concentrated solution was adjusted to ~3 with adding few 0.01 M HCl. Then, 1 mL of the concentrated solution mixed with 0.2 mL of d₆-DMSO was used for ¹H NMR spectroscopy measurement.

Theoretical calculations:

In DFT calculations, we employed projector-augmented waves (PAW)^{40, 41} generalized gradient approximation (GGA).⁴²⁻⁴⁴ In the plane wave calculations, cutoff energy of 500 eV was applied, which was automatically set by the total energy convergence calculation for 1T-MoS₂ slab systems. DFT simulations were performed based on the unit cell of 1T-MoS₂ system shown in **Figure S12-15**.⁴⁵ The dimension of unit cell of $a = b = 3.19 \text{ \AA}$, $c = 5.945 \text{ \AA}$, and $\alpha = \beta = 90^\circ$, $\gamma = 120^\circ$. Initially, the 1T-MoS₂ was constructed to consist of 1T-MoS₂ unit cell structure containing one Mo atoms with one S atoms; the system was then allowed to reach its lowest energy configuration by a relaxation procedure. For these calculations, a $3 \times 3 \times 1$ *k*-Point mesh was used in the super cell. The atoms in the cell were allowed to relax until the forces on unconstrained atoms are less than 0.01 eV/Å. The adsorption energy in N₂-1T-MoS₂ system, E_{ad} , is defined as the sum of interactions between the capping molecule and slab system, and it is given as $E_{ad} = E_{total} - E_{MoS_2} - (E_{N_2})$, where E_{total} , E_{MoS_2} and E_{N_2} are the total energy of the system, 1T-MoS₂ system energy, and the single N₂ molecule energy. The negative sign of E_{ad} corresponds to the energy gain of the system due to molecular adsorption.

Supporting Information.

Additional XRD patterns, SEM images, time dependent curves, UV spectra, calibration graphs, in-situ XRD set-up and theoretical considerations.

Notes:

The authors declare no conflict of interest.

Author Contributions

S. Patil and D. Wang conceived the project and designed the experiments. S. Patil, Y. Chen, C. Chang, S. Li, Y. Lee and Y. Lai performed material preparation, structural characterization and electrochemical measurements. S. Hsieh, and C. Chen helped to perform the X-ray photoemission measurement in the NSRRC. H. Chou helped to perform DFT simulation. Y. Lin, Hsin Li and Y. Chang helped to do NMR measurement. S. Patil and D. Wang co-wrote the paper. All authors discussed the results and commented on the manuscript.

Acknowledgements

This work has been financially supported by the Ministry of Science and Technology of Taiwan (MOST 106-2113-M-029-006-MY2, MOST 106-2632-M-029-001 and MOST 107-2622-M-029-001-CC2) and Tunghai University. We thank Dr. U-Ser Jeng for assistance at beamline BL23A at Taiwan Light Source (TLS) and Dr. Hwo-Shuenn Sheu, Dr. Yu-Chun Chuang for assistance at beamline 09A at the Taiwan Photon Source (TPS).

References:

1. T. Oshikiri, K. Ueno and H. Misawa, *Angewandte Chemie International Edition*, 2016, **55**, 3942-3946.
2. V. Rosca, M. Duca, M. T. de Groot and M. T. Koper, *Chemical Reviews*, 2009, **109**, 2209-2244.
3. R. F. Service, *Science (New York, NY)*, 2014, **345**, 610.
4. C. Guo, J. Ran, A. Vasileff and S.-Z. Qiao, *Energy & Environmental Science*, 2018, **11**, 45-56.
5. X. Cui, C. Tang and Q. Zhang, *Advanced Energy Materials*, 2018, **8**, 1800369.
6. Z. Yan, M. Ji, J. Xia and H. Zhu, *Advanced Energy Materials*, 2019, 1902020.
7. Y.-C. Hao, Y. Guo, L.-W. Chen, M. Shu, X.-Y. Wang, T.-A. Bu, W.-Y. Gao, N. Zhang, X. Su and X. Feng, *Nature Catalysis*, 2019, **2**, 448-456.
8. S. Dou, X. Wang and S. Wang, *Small Methods*, 2019, **3**, 1800211.
9. G. F. Chen, S. Ren, L. Zhang, H. Cheng, Y. Luo, K. Zhu, L. X. Ding and H. Wang, *Small Methods*, 2019, **3**, 1800337.
10. J. Zhang, X. Tian, M. Liu, H. Guo, J. Zhou, Q. Fang, Z. Liu, Q. Wu and J. Lou, *Journal of the American Chemical Society*, 2019, **141**, 19269-19275.
11. C. C. Chang, S. R. Li, H. L. Chou, Y. C. Lee, S. Patil, Y. S. Lin, C. C. Chang, Y. J. Chang and D. Y. Wang, *Small*, 2019, **15**, 1904723.

12. P. Li, W. Fu, P. Zhuang, Y. Cao, C. Tang, A. B. Watson, P. Dong, J. Shen and M. Ye, *Small*, 2019, **15**, 1902535.
13. K. C. MacLeod and P. L. Holland, *Nature chemistry*, 2013, **5**, 559.
14. X. Guo, H. Du, F. Qu and J. Li, *Journal of Materials Chemistry A*, 2019, **7**, 3531-3543.
15. S. B. Patil and D. Y. Wang, *Small*, 2020, 2002885.
16. L. Zhang, X. Ji, X. Ren, Y. Ma, X. Shi, Z. Tian, A. M. Asiri, L. Chen, B. Tang and X. Sun, *Advanced Materials*, 2018, **30**, 1800191.
17. B. H. Suryanto, D. Wang, L. M. Azofra, M. Harb, L. Cavallo, R. Jalili, D. R. Mitchell, M. Chatti and D. R. MacFarlane, *ACS Energy Letters*, 2018, **4**, 430-435.
18. Y. Qiu, X. Peng, F. Lü, Y. Mi, L. Zhuo, J. Ren, X. Liu and J. Luo, *Chemistry—An Asian Journal*, 2019, **14**, 2770-2779.
19. L. Han, X. Liu, J. Chen, R. Lin, H. Liu, F. Lü, S. Bak, Z. Liang, S. Zhao and E. Stavitski, *Angewandte Chemie*, 2019, **131**, 2343-2347.
20. M. M. Shi, D. Bao, S. J. Li, B. R. Wulan, J. M. Yan and Q. Jiang, *Advanced Energy Materials*, 2018, **8**, 1800124.
21. S. J. Li, D. Bao, M. M. Shi, B. R. Wulan, J. M. Yan and Q. Jiang, *Advanced materials*, 2017, **29**, 1700001.
22. X. Geng, W. Sun, W. Wu, B. Chen, A. Al-Hilo, M. Benamara, H. Zhu, F. Watanabe, J. Cui and T.-p. Chen, *Nature communications*, 2016, **7**, 1-7.
23. M. A. Lukowski, A. S. Daniel, F. Meng, A. Forticaux, L. Li and S. Jin, *Journal of the American Chemical Society*, 2013, **135**, 10274-10277.
24. M. Acerce, D. Voiry and M. Chhowalla, *Nature nanotechnology*, 2015, **10**, 313.
25. J. He, G. Hartmann, M. Lee, G. S. Hwang, Y. Chen and A. Manthiram, *Energy & Environmental Science*, 2019, **12**, 344-350.
26. Y. Liu, M. Han, Q. Xiong, S. Zhang, C. Zhao, W. Gong, G. Wang, H. Zhang and H. Zhao, *Advanced Energy Materials*, 2019, **9**, 1803935.
27. C. Tsai, H. Li, S. Park, J. Park, H. S. Han, J. K. Nørskov, X. Zheng and F. Abild-Pedersen, *Nature communications*, 2017, **8**, 1-8.
28. B. Seo and S. H. Joo, *Nano Convergence*, 2017, **4**, 1-11.
29. C.-H. Lee, S. Lee, Y.-K. Lee, Y. C. Jung, Y.-I. Ko, D. C. Lee and H.-I. Joh, *ACS Catalysis*, 2018, **8**, 5221-5227.
30. T. Xiang, Q. Fang, H. Xie, C. Wu, C. Wang, Y. Zhou, D. Liu, S. Chen, A. Khalil and S. Tao, *Nanoscale*, 2017, **9**, 6975-6983.
31. N. H. Attanayake, A. C. Thenuwara, A. Patra, Y. V. Aulin, T. M. Tran, H. Chakraborty, E. Borguet, M. L. Klein, J. P. Perdew and D. R. Strongin, *ACS Energy Letters*, 2017, **3**, 7-13.
32. D. Yang, S. J. Sandoval, W. Divigalpitiya, J. Irwin and R. Frindt, *Physical Review B*, 1991, **43**, 12053.
33. Y. Li, H. Wang, L. Xie, Y. Liang, G. Hong and H. Dai, *Journal of the American Chemical Society*, 2011, **133**, 7296-7299.
34. L. Wu, N. Y. Dzade, M. Yu, B. Mezari, A. J. van Hoof, H. Friedrich, N. H. de Leeuw, E. J. Hensen and J. P. Hofmann, *ACS energy letters*, 2019, **4**, 1733-1740.
35. C. D. Quilty, L. M. Housel, D. C. Bock, M. R. Dunkin, L. Wang, D. M. Lutz, A. Abraham, A. M. Bruck, E. S. Takeuchi and K. J. Takeuchi, *ACS Applied Energy Materials*, 2019, **2**, 7635-7646.
36. H.-J. Liao, Y.-M. Chen, Y.-T. Kao, J.-Y. An, Y.-H. Lai and D.-Y. Wang, *The Journal of Physical Chemistry C*, 2017, **121**, 24463-24469.
37. S. Z. Andersen, V. Čolić, S. Yang, J. A. Schwalbe, A. C. Nielander, J. M. McEnaney, K. Enemark-Rasmussen, J. G. Baker, A. R. Singh and B. A. Rohr, *Nature*, 2019, **570**, 504-508.
38. C. Li, S. Mou, X. Zhu, F. Wang, Y. Wang, Y. Qiao, X. Shi, Y. Luo, B. Zheng and Q. Li, *Chemical Communications*, 2019, **55**, 14474-14477.

39. G. W. Watt and J. D. Crisp, *Analytical Chemistry*, 1952, **24**, 2006-2008.
40. D. Vanderbilt, *Physical review B*, 1990, **41**, 7892.
41. M. C. Payne, M. P. Teter, D. C. Allan, T. Arias and a. J. Joannopoulos, *Reviews of modern physics*, 1992, **64**, 1045.
42. J. P. Perdew, J. A. Chevary, S. H. Vosko, K. A. Jackson, M. R. Pederson, D. J. Singh and C. Fiolhais, *Physical review B*, 1992, **46**, 6671.
43. G. Kresse and J. Hafner, *Phys. Rev. B*, 1996, **54**, 11169.
44. G. Kresse and D. Joubert, *Physical review b*, 1999, **59**, 1758.
45. T. Hu, R. Li and J. Dong, *The Journal of chemical physics*, 2013, **139**, 174702.

Figures:

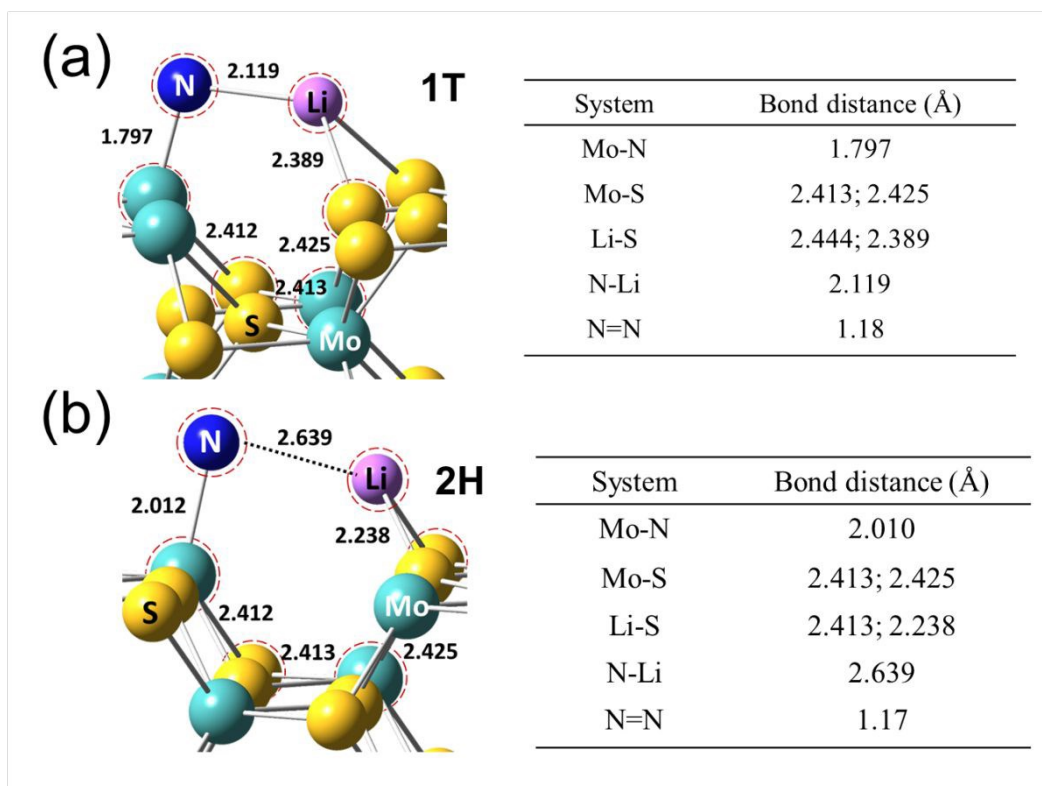


Figure 1. The optimized configuration of pseudo six-member ring on (a) 1T-MoS₂ and (b) 2H-MoS₂ with Li-S interactions which consisted of the link of N...Li...S—Mo—S—Mo, respectively. The corresponding bond distances were provided on the right part of figures.

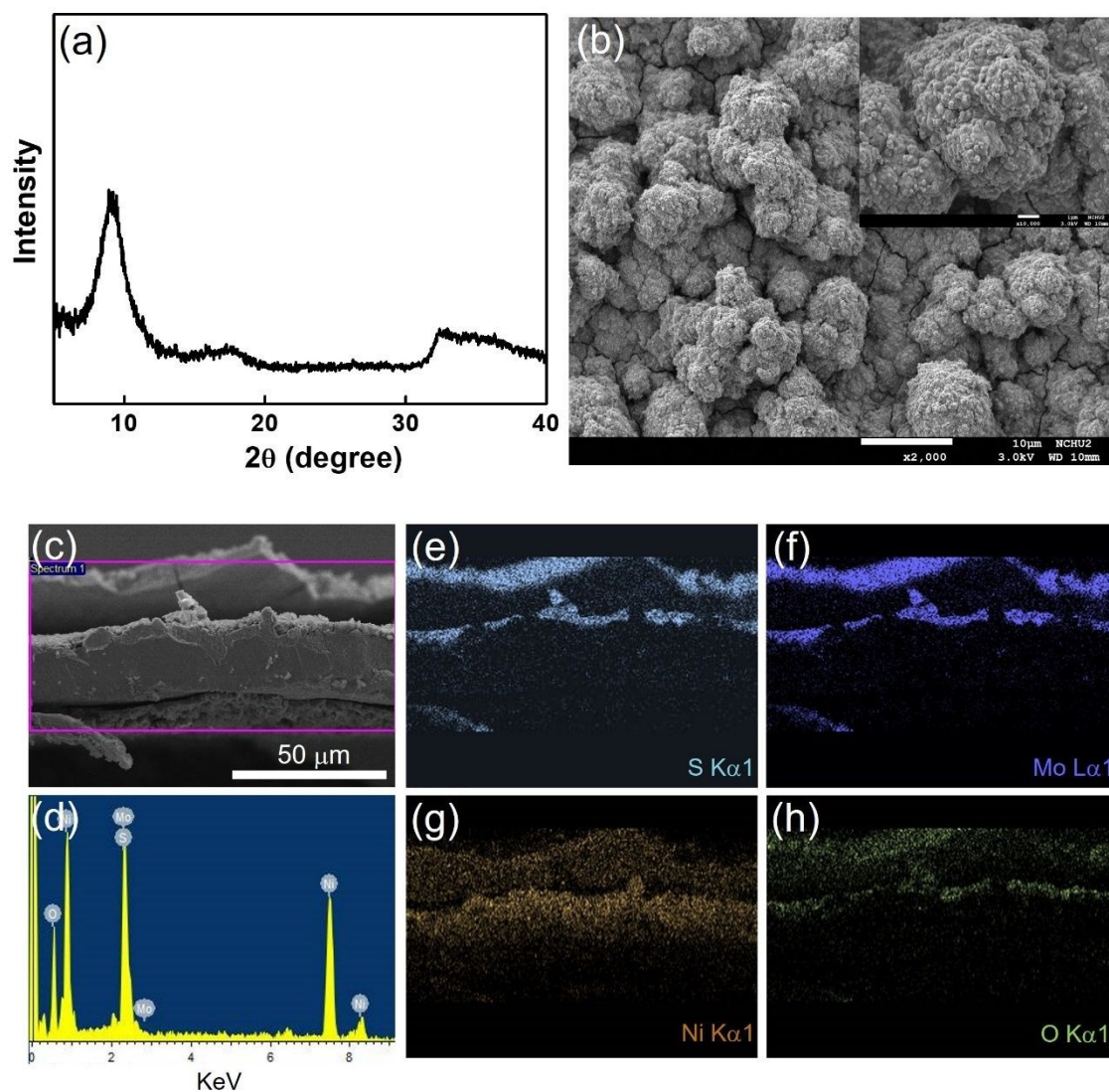


Figure 2. (a) The XRD pattern of 1T-MoS₂-Ni. (b) The SEM image of 1T-MoS₂-Ni. The amplification image was shown in the inset. (c) Cross section SEM image and (d) related EDX spectrum of 1T-MoS₂-Ni. Elemental mapping of (e) S atom, (f) Mo atom, (g) Ni atom and (h) O atom of 1T-MoS₂-Ni.

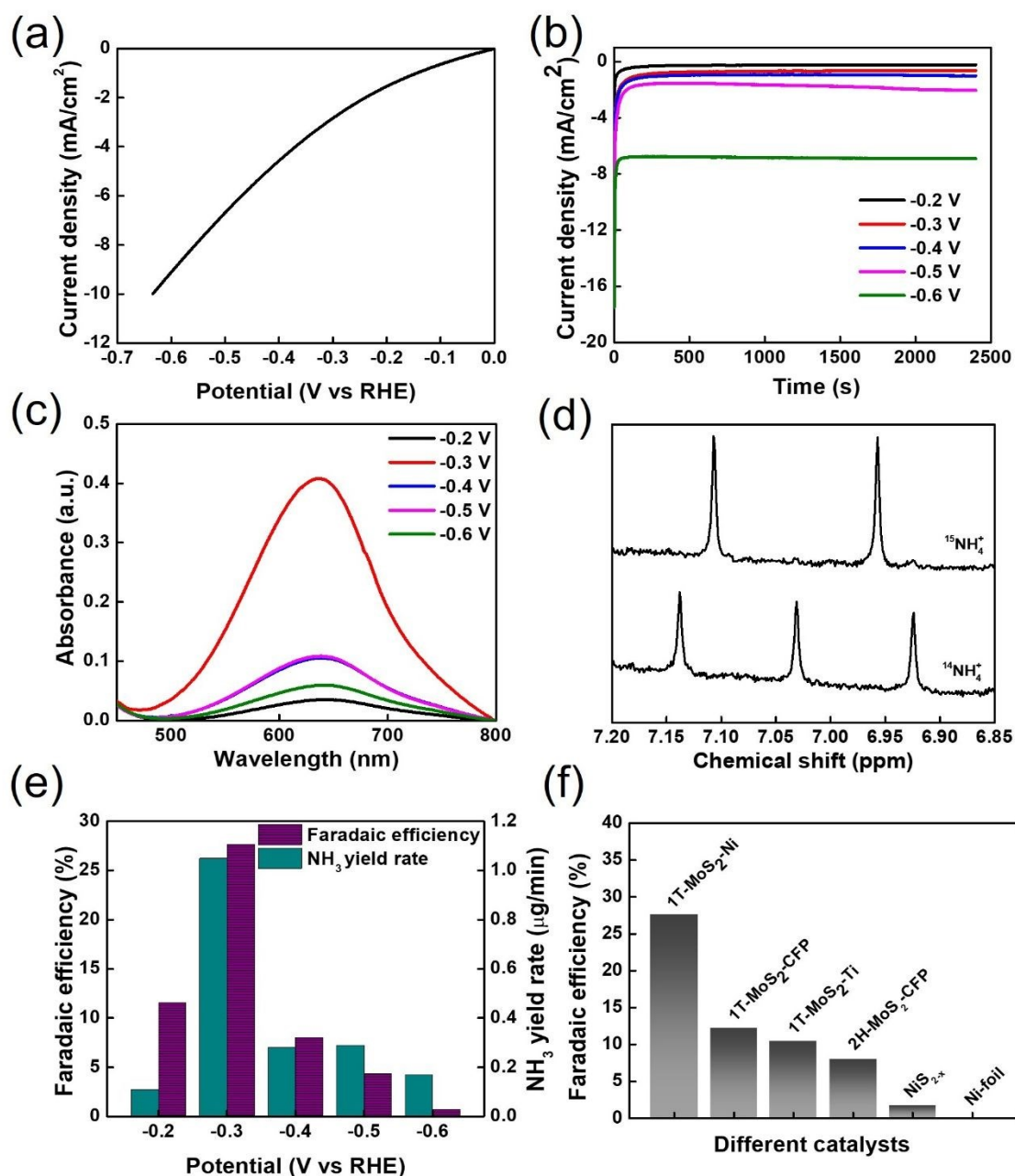


Figure 3. (a) Linear sweep voltammetry of 1T-MoS₂-Ni operated in N₂-saturated 0.25 M LiClO₄ electrolyte. (b) Time dependent current curves of 1T-MoS₂-Ni at different potential (-0.2 to -0.6 V v.s. RHE) in N₂-saturated 0.25M LiClO₄. (c) UV-vis absorption spectra of the electrolytes colored with indophenol indicator at a series of potentials for 40 min. (d) ¹H NMR spectrum of the yielded ¹⁵NH₄⁺ and ¹⁴NH₄⁺ after NRR electrolysis at -0.3V using ¹⁵N₂ and ¹⁴N₂ as feeding gases, respectively. (e) Faradaic efficiency and respective NH₃ yield rate of 1T-MoS₂-Ni at different potentials. (f) Faradaic efficiency of different materials tested at -0.3 V in 0.25 M LiClO₄ electrolyte.

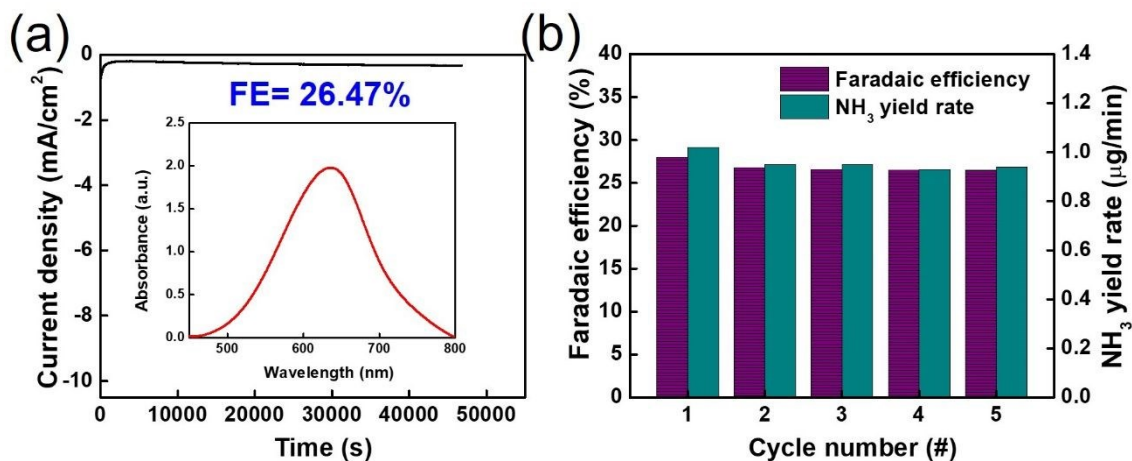


Figure 4. (a) Time dependent current curves of 1T-MoS₂-Ni over 13h (inset: UV-vis absorption spectra of the electrolyte stained with indophenol indicator after NRR electrolysis for 13h). (b) Faradaic efficiency and respective NH₃ yield rate of 1T-MoS₂-Ni for consecutive 5 cycles (40 min each).

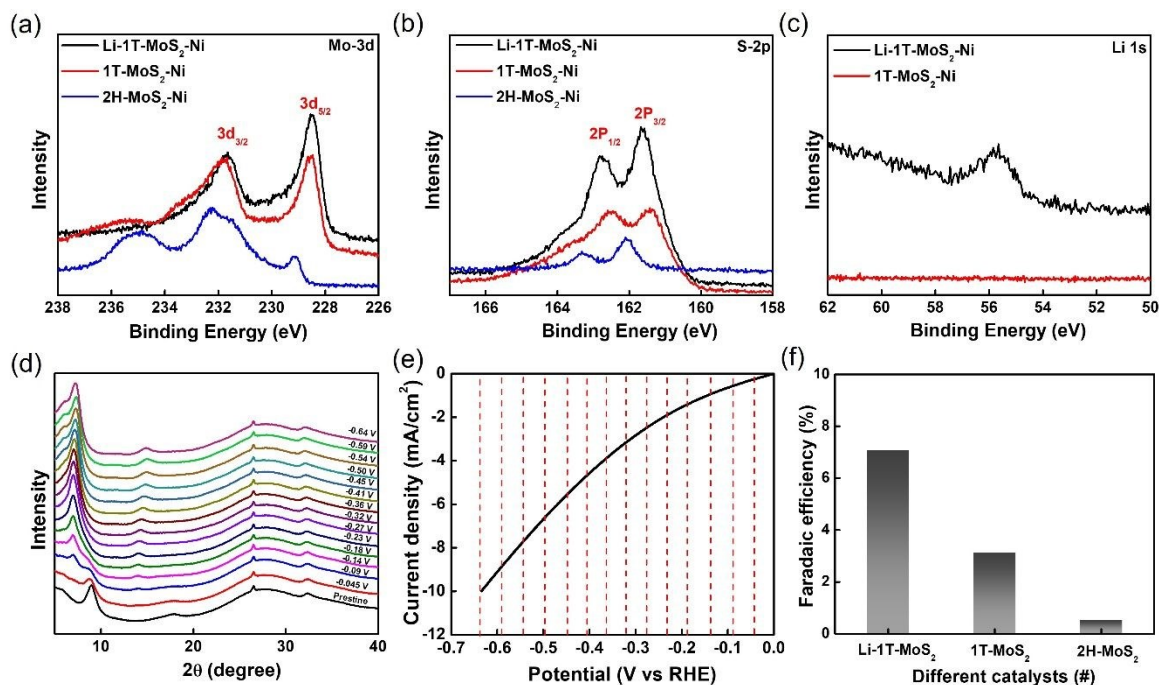


Figure 5. (a) Mo-3d, (b) S-2p and (c) Li-1s XPS spectra of Li-1T-MoS₂-Ni, intrinsic 1T-MoS₂ and 2H-MoS₂, respectively. (d) In-situ XRD patterns of representative 1T-MoS₂-CFP collected during operation of NRR in the LiClO₄ electrolyte with a scan rate of 0.5 mV from 0 to -0.6 V. (e) The corresponding linear scan voltammetry of 1T-MoS₂-CFP for in-situ XRD measurement. The XRD spectra were collected from each voltage (red dashed line), as shown in Figure 3 (d). (f) Faradaic efficiency of different catalysts at -0.3V in 0.5 M Na₂SO₄ electrolyte.

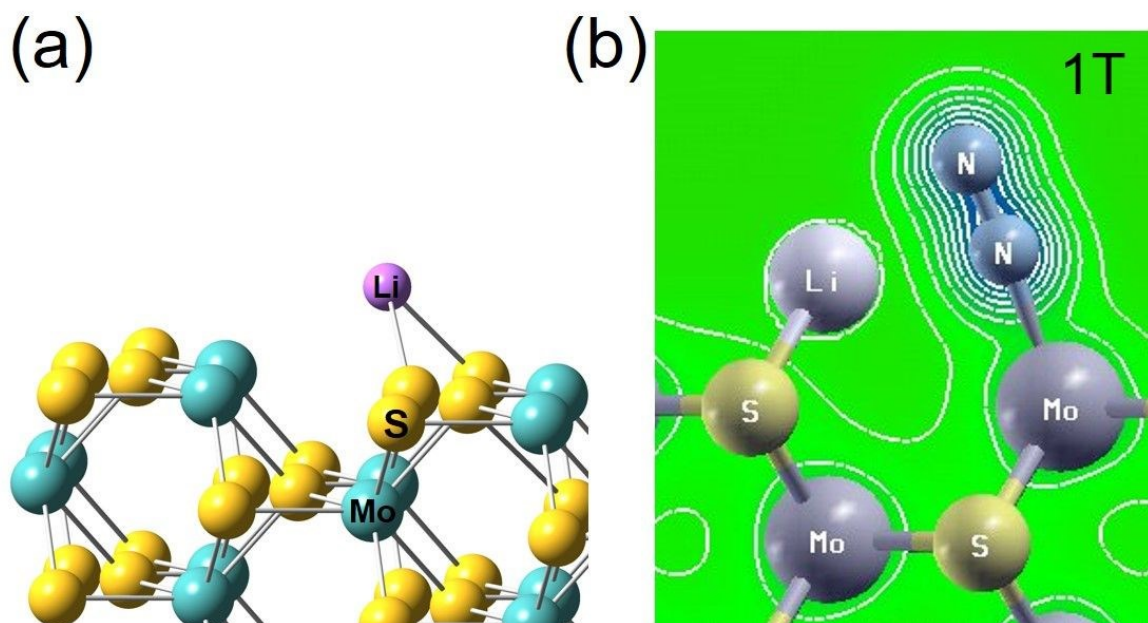


Figure 6. (a) The models of side-view of Li-1T-MoS₂ slab surface with a formation of Li-S bond. (b) The representative electron contour map of intermediates N₂ adsorbed on Mo atom of Li-1T-MoS₂.

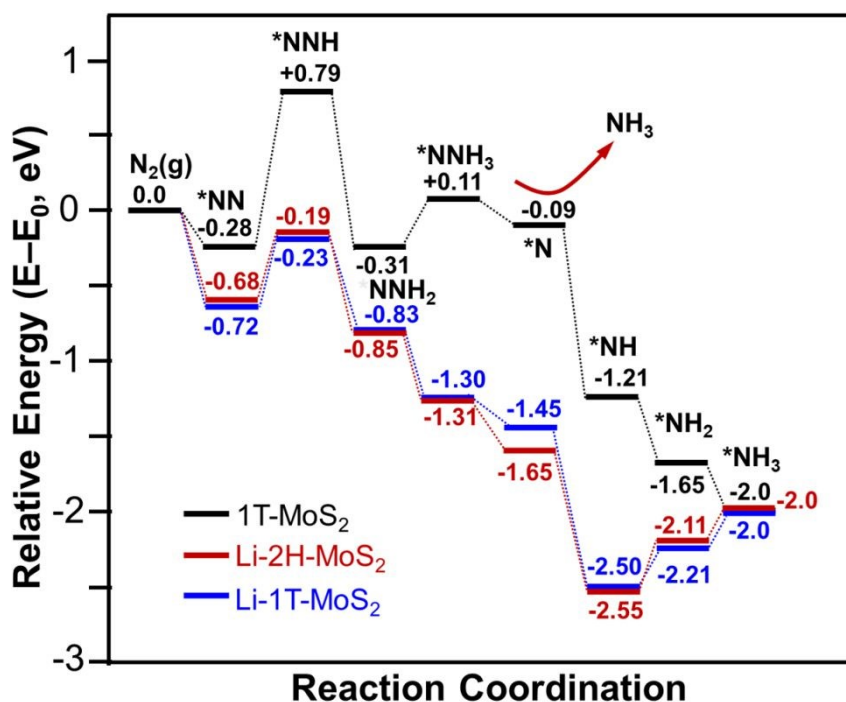


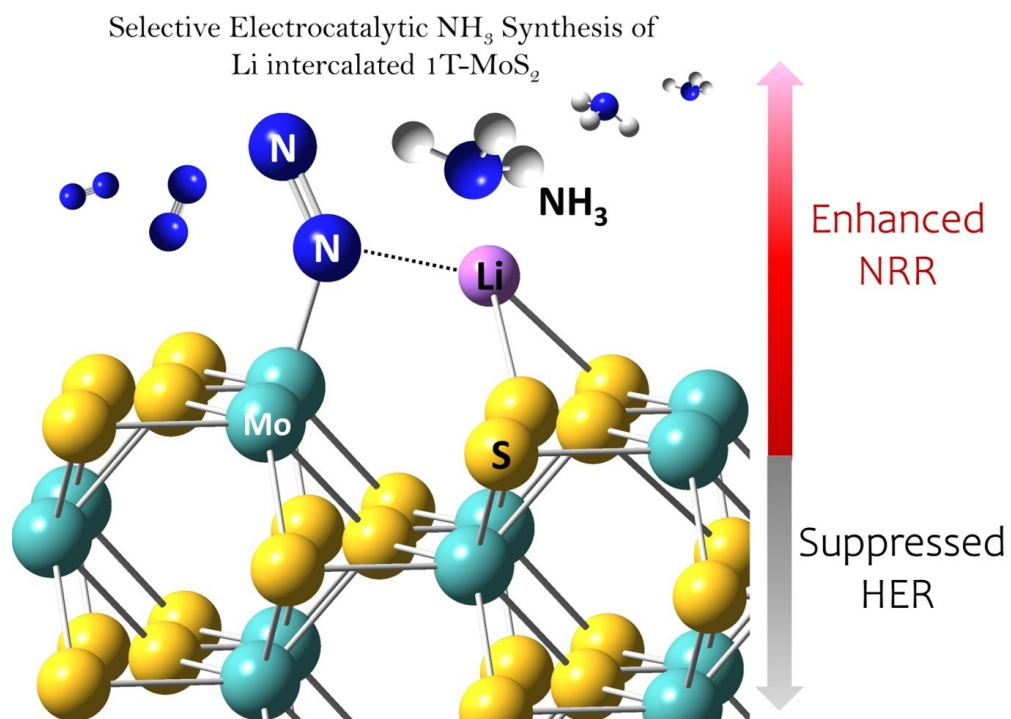
Figure 7. Potential energy diagram for NRR at intrinsic 1T-MoS₂, Li-1T-MoS₂ and Li-2H-MoS₂. An asterisk (*) denoted as the adsorption site.

Table 1. Adsorption energies and optimized geometries calculation of N₂ in Li-1T-MoS₂ and Li-2H-MoS₂ systems

System	E _{ad} (eV)	Distance (Mo-N) (Å)	Distance (N-N) (Å)	Distance (Li-S) (Å)	Distance (Li-N) (Å)	Distance (Mo-S) (Å)
Mo site of 1T-MoS ₂	-0.28	1.801	1.174			2.412; 2.424
S site of 1T-MoS ₂	+3.2					
Mo site of Li-1T-MoS ₂	-0.72	1.797	1.181	2.444; 2.389	2.119	2.413; 2.425
Mo site of Li-2H-MoS ₂	-0.70	2.010	1.172	2.413; 2.238	2.639	2.413; 2.425

Table 2. Bader Charge Analysis of N₂ adsorption on 1T-MoS₂ with Li-S interactions

Species	Charge (e)	Charge difference (e)
MoS₂	Mo: 4.70	
	S1: 6.80	
	S1: 6.80	
N₂	N: 6.87	
Li	L: 3.61	
1T-MoS₂ with Li	Mo (edge): 4.38	Mo (edge): 4.38 - 4.70 = -0.32
	S1 (edge): 6.90	S1 (edge): 6.90 - 6.80 = +0.10
	S2 (edge): 6.96	S2 (edge): 6.96 - 3.73 = +0.23
	Li: 2.16	Li: 2.16 - 3.61 = -1.45
	N: 6.98	N: 6.98 - 6.87 = +0.11



232x168mm (149 x 149 DPI)